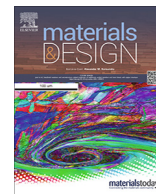# Insight into microstructure and flexural strength of ultra-high temperature ceramics enriched SICARBON™ composite

Pietro Galizia, Diletta Sciti, Neraj Jain

Insight into microstructure and flexural strength of ultra-high temperature ceramics enriched SICARBON™ composite

Pietro Galizia [a],[*], Diletta Sciti [a], Neraj Jain [b]

[a] CNR-ISTEC, National Research Council of Italy – Institute of Science and Technology for Ceramics, Via Granarolo 64, I-48018 Faenza, Italy
[b] Institute of Structures and Design, German Aerospace Center, Pfaffenwaldring 38-40, 70569 Stuttgart, Germany

HIGHLIGHTS

- Strength of 370 MPa was obtained by tilting the beams from the lay-up configuration.
- Tilted beams gave valid strength values even with a span-to-thickness ratio of 10.
- Failure onset of 280 MPa was obtained through the maximum proportional limit stress.
- Elastic constants and Tsai-Wu failure indices were predicted using material genome
- UHTC enrichment did not affect strength and strain to failure (1%) of the well-developed SICARBON™.

GRAPHICAL ABSTRACT
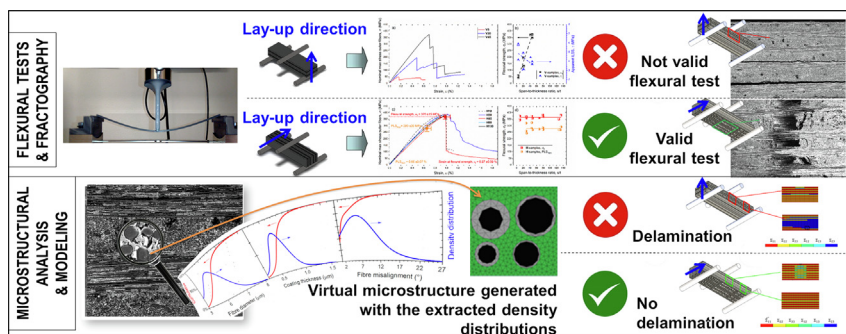
ARTICLE INFO

ABSTRACT

Research efforts on Ceramic Matrix Composites (CMCs) are aimed to increase the operating temperature in oxidizing environments by adding Ultra-High Temperature Ceramic (UHTC) phases to the matrix. The structural performances of UHTC-enriched CMCs are generally investigated through bending test because it requires simple fixture and specimen geometry with small quantity of plate material. However, there are hardly any scientific studies which bring out what bending test conditions are required to determine reliable flexural strength of these composites. In this study, the effect of span length and specimen orientation on the flexural strength of UHTC-enriched SICARBON™ material, produced by Airbus, was comprehensively evaluated and reported. Transition of the failure mode was obtained by tilting the specimens with horizontal build direction instead of lay-up configuration (vertical build direction). The tilted configuration allowed to get a valid flexural strength of 370 MPa even with small specimens of about 30 mm. To assess failure mode in different test configurations, virtual microstructure was generated on the base of cumulative distribution functions of observed microstructural features. Tsai-Wu failure criterion was extended in order to evaluate direction dependent failure indices for different lay-up configurations.

1. Introduction

Ceramic Matrix Composites (CMC) are setting foot in the future aerospace transportation by replacing superalloys components of hypersonic and rocket engines [1–3]. For instance during hyper-

* Corresponding author.
   E-mail address: pietro.galizia@istec.cnr.it (P. Galizia).

sonic flight, sharp leading edges of engine parts (engine cowl lip) and main body (nose and fins) should exceed 2000 °C to further increase the fuel-efficiency, reduce the exhaust emissions and save cost [4]. In these components, where cooling is impractical, the choice from the options of ceramic matrix narrows down to a limited number of diborides of transition metals, for example ZrB_2, which shows typical non-ablative properties and refractory behaviour of ultra-high temperature ceramics (UHTC) [5–10]. The so called ultra-high ceramic matrix composites (UHTCMC) are paving the way for reusable vehicles/engines for sustained hypersonic flights [11–22]. This new class of materials, based on UHTC matrices reinforced with carbon or silicon carbide fibres, was developed in the H2020 European project C³harme (Next Generation Ceramic Composites For Combustion Harsh Environments And Space, GA n. 685594) [23]. Unlike bulk UHTCs, UHTCMCs are damage-tolerant and notch-insensitive [24–27]. However, the production of large and dense UHTCMCs is extremely challenging [16,28–31]. This issue is often addressed by adding UHTC or metal precursor (metal derived UHTC) powders into conventional CMCs, e.g. C_f/SiC, fabricated via Polymer-Infiltration-Pyrolysis (PIP) [32–38] or chemical vapor infiltration [39–43]. However, CMCs with unidirectional 0°-90°, 2D or even 2.5 D and 3D architectures are weak along the transverse direction and are prone to exhibit 'splitting failure' [44–49]. The weakness is due to the higher matrix porosity and lower grain cohesion, with respect to that of sintered UHTC matrix, and to the delamination defects that occur mainly during the pyrolysis (especially in case of plates thicker than 5 mm) [50]. Both experimental investigations and finite element analysis showed that C_f/SiC specimens fail under interlaminar shear stress, and only at the end, final bending failure occurs [50]. The facile 'splitting failure' can be exploited to measure the interlaminar shear strength (ILSS) through the short beam shear test (SBT) method. SBT is the chief method for determining ILSS of laminates composites and has the great advantage of its simplicity with respect to the other ILSS test methods (such as double-notched tension), which involve complex fixtures and extensive machining [51]. Usually, only an "apparent" ILSS as function of span-to-thickness ratio (s/t) is possible to measure through SBT. In fact, owing to the large compressive stresses in the areas near the loading and support cylinders, no pure shear state of stress is realized with SBT [52,53]. However, less literature is found considering the interlaminar properties of UHTC-enriched C_f/SiC [50]. On the other hand, the low ILSS of planar CMCs led to lack of accurate and reliable flexural test results [54]. In fact, the tendency to 'splitting' failure can lead to underestimation of the flexural strength (σ_f) or, in the worst-case scenario, to a pure interlaminar failure that makes the determination of σ_f impossible. Nevertheless, bending test of UHTC-enriched C_f/SiC are generally performed with a s/t value smaller than 17. This value is quite smaller than the value of 32 suggested as starting point in the ASTM C1341 – 13 standard in order to limit the interlaminar shear contribution to the failure. Moreover, to the best of our knowledge, no bending tests of UHTC-enriched C_f/SiC were carried out under edge-loading or with tilted specimens with horizontal build direction instead of lay-up configuration (vertical build direction). This bending configuration is particularly useful in the case of cross-ply architecture because it not only avoids the interlaminar shear failure owing to the reduced critical tensile stress but also simplify the analytical modelling of the flexural strength to calculate the effective contribution of the 90° plies to the flexural strength [55].

In this work, ILSS and σ_f of UHTC-enriched SICARBON™ material produced by Airbus (former EADS) [34,56,57] were investigated through bending tests by (i) gradually increasing s/t ratio up to 130 and (ii) changing layers orientation (horizontal or vertical build direction). The main aim, beyond measuring the ILSS and σ_f of this new material, was to find the bending setup necessary to obtain a valid test and a reliable flexural strength. Hence, this study would offer a guideline to optimize the test configurations in the future for determination of valid strength of CMCs while limiting the quantity of material required for testing. We chose this material because SICARBON™ is already a well-developed product and the addition of UHTC within the C_f/SiC composites is the current research effort carried on increasing the temperature limit. An extensive image analysis on electron micrographs was performed to measure the volume content of the constitutive phases and to extract the cumulative distribution function of the characterising microstructural features, such as fibre diameter and misalignment. The microstructural characterization was reported as single values of the measured volumetric contents and as parameters of an appropriately modified Boltzmann function to consider, at most, two populations in the fitted distributions. The reported microstructural framework would offer a sort of microstructural genome that can be easily integrated in the models [58]. Young's modulus of the composite was estimated by integrating the microstructural genome into the classical laminate theory. A good agreement between the experimental modulus and the calculated one was found by considering the large content of porosity and pyrolytic carbon. Finally, with the help of direction dependent extension of Tsai Wu failure criterion [59], the load carrying limit of the samples and the responsible failure modes were evaluated.

2. Method

2.1. Material manufacturing

Unwound C_f/SiC composites enriched of ZrB_2 and TaC UHTC were fabricated via the filament winding and PIP process developed by Airbus (former EADS) [56] and currently used to manufacture the SICARBON™ material [57]. A schematic overview of the involved process is displayed in Fig. 1 . The following single steps of PIP-process are:

1) Continuous carbon fibres (type T800HB-6000-40B, Toray Industries Inc., Japan, tensile strength of 5490 MPa, modulus of elongation of 294 GPa, strain at failure of 1.9%, density of 1.81 g/cm³, filament diameter of about 5 μm) were coated with pyrolytic carbon (PyC) via CVD to avoid fibre–matrix reaction.
2) Coated fibre bundles were infiltrated with pre-ceramic slurry during an automatized filament winding technique. The slurry was prepared by wet mixing pre-ceramic polymer, ZrB_2 powder (Grade B, HC Starck, Germany) and Ta powder (American Elements, California, US). The starting amount of pre-ceramic polymer and fillers was the same as used for Z50 sample reported in Ref. [34].
3) Greenbody samples were prepared by staking 16 prepregs of 185 mm × 160 mm surface in a $[0,90]_{4s}$ laminate.
4) Curing was done in the autoclave at 100–300 °C under 10–20 bar.
5) Ceramization via pyrolysis was performed at 1600 °C in nitrogen atmosphere at ambient pressure.
6) 3 re-infiltration steps with a pre-ceramic SiC precursor and following pyrolysis was carried out with the aim to reduce the porosity resulted from the conversion of the organic to thenon-organic state. The resulted plate had a thickness of 3.7 mm.
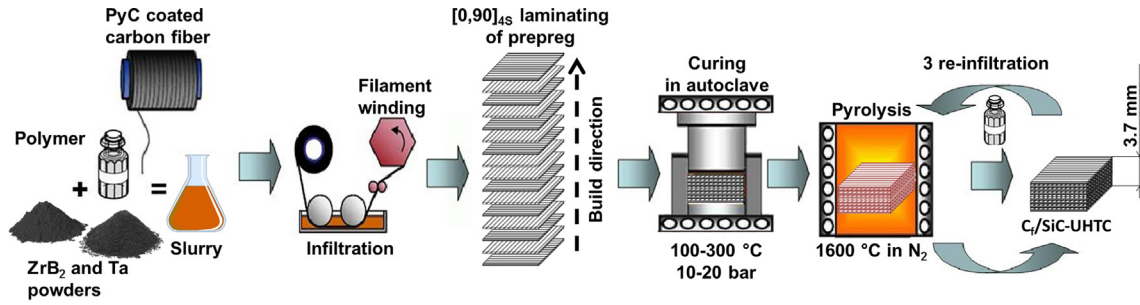
Fig. 1. Schematic flowchart of filament winding and Polymer-Infiltration-Pyrolysis (PIP) process developed by EADS [56] and modified to manufacture unwound C$_f$/SiC composites enriched of ZrB$_2$ and TaC UHTC.

2.2. Characterization

2.2.1. Microstructure

The geometric density was measured on the fabricated plate of $185 \times 160 \times 3.7$ mm^3. The microstructures were analysed on polished and fractured surfaces using field emission scanning electron microscopy (FE-SEM, Carl Zeiss Sigma NTS GmbH Oberkochen, Germany). Volumetric content of UHTC, SiC, fibre (V_f) and coating, and distribution of fibre diameter (D) and coating thickness (T) were measured by image analysis using the Image-Pro Analyzer 7.0 software (v.7, Media Cybernetics, USA) on FE-SEM images of polished sections. D was calculated as equivalent circular area diameter. T was calculated as half the difference between equivalent circular area diameter of the coated fiber and that of the fiber without considering the coating. Distribution of fibre misalignment (θ), size of SiC particles (P) and aggregates (B) were measured on fractured surfaces. The cumulative distribution functions (CDF) of the microstructural features measured through image analysis were fitted with the following modified Boltzmann equation to consider, at most, two intended populations:

$$F(x) = 1 + \frac{p_1(1+b_1)}{1+e^{\frac{x-x_1}{a_1}}} + b_2 + \frac{(1-p_1)}{1+e^{\frac{x-x_2}{a_2}}} \tag{1}$$

where x is the generic microstructural quantity (D, T, θ, B or P), x_1 and x_2 are the corresponding median values (50th percentile), p_1 is the fraction of the first population, a_1 and a_2 define the steepness of the 1°- and 2°-distribution, respectively (a larger absolute value denotes a shallow curve), and b_1 and b_2 are the parameter values that can be associated to the fraction. Ideally b1 and b2 should be equal to -2 and 0, respectively, in case there is only one population, and to 0 and -1, respectively, if two populations are considered. However, in certain cases we did not fix b_1 and b_2 to better fit the measured data (achieve a R^2 > 0.99). It is worth noting that the extrapolated parameter values not only were useful for the modelling presented in this work but also offer an initial microstructural genome [58] of the investigated materials, which is useful for dissemination purpose and facilitation of discovery, modelling and design of this class of composites.

2.2.2. Mechanical properties

The Young's modulus of the composite (E_c) was measured using the resonance frequency method (ASTM C1198 - 09) on three bars $2.5 \times 7 \times 60$ mm^3 (thickness by width by length, respectively).

The labels and dimensions of specimens and each corresponding bending test configuration are reported in Table 1 and Fig. 2, respectively. The sample ID indicates how the build direction was oriented during bending test: vertical (V) and horizontal (H), while the number represents the s/t ratio. All tests were performed in air at room temperature using a Zwick-Roell Z050 screw-driven load frame, support and loading cylinders of 3 mm in diameter. A

strain rate of 0.0001 s^{-1}, calculated according to ASTM C1341 – 13 standard, was set. Three specimens were fractured for each configuration. s/t was varied from 5 to 130 in order to (i) reduce the departure of stress distribution from the classical beam theory and measure a more reliable ILSS value [52] and (ii) try to observe a transition of the failure mode from shear failure to tensile or compression failure. The transition occurs when s/t ratio satisfies the Eq. (2), otherwise the larger s/t ratio allows just to achieve a higher maximum flexural stress (σ) that is even more closer to the flexural strength (σ_f, the critical stress level to initiate the failure in tension or compression).

$$s/t > 2\sigma_f/ILSS \tag{2}$$

To increase the chances of getting a valid flexural fracture, three-point bending tests were performed with specimens having horizontal build direction (Fig. 2c, d). Horizontal build direction imposing the *iso*-strain condition lowers the flexural strength due to the presence of both 0° and 90° fibres in the tensile surface where the maximum tensile strain is achieved, hence also $\sigma_f/ILSS$ could be lowered. ILSS for both four- and three-point test was calculated with Eq. (3) according to the classic beam theory [60]:

$$ILSS = 3P/4wt \tag{3}$$

where P is the total applied force (the first peak load in the bending test), and *w* and *t* are average measured width and thickness of the specimen, respectively. According to ASTM C1341 – 13, flexural strength was calculated with Eqs. (4) and (5) for three- and four-point bending test, respectively.

$$\sigma_f = 3sP\left[1 + 6(d/s)^2 - 4t(d/s^2)\right]/2wt^2 \tag{4}$$

$$\sigma_f = 3sP/4wt^2 \tag{5}$$

where d is the deflection at beam centre at maximum applied force and the term between the square bracket of Eq. (4) considers the nonlinear behaviour due to the large s/t ratio. The maximum proportional limit stress/strain (PLS$_{max}$) was defined as the stress at 5% deviation from the linear segment extrapolated from the range where the slope was maximum. Four-point bending configuration of V5-specimens (Fig. 2a) was chosen in order to achieve a direct comparison with previously characterized continuous fibre-reinforced ultra-high temperature ceramics [24–26,44]. The maximum lower spans used for V45 and H130 were limited by the length of the specimens and the maximum deflection allowed by the fixture. The intermediate spans were chosen randomly. The strain (ε) was estimated according to ASTM C1341 – 13 standard to compare the load-displacement curves obtained with different test configurations (Fig. 2).

Table 1
Sample ID and corresponding geometry and bending configuration.

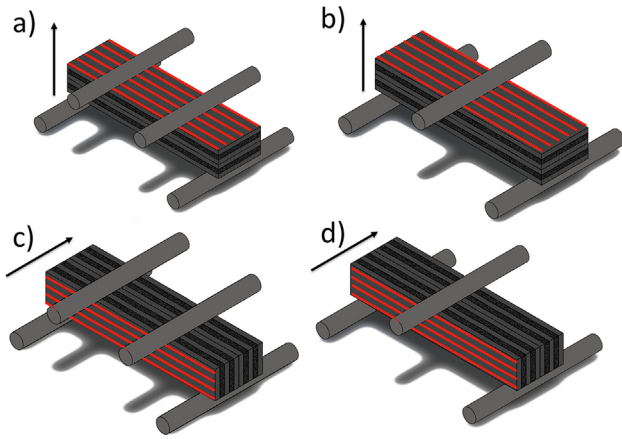| ID	Sample geometry		Bending set up			Sketch
	Thickness	Width	pt	Upper span	Lower span	
	(mm)	(mm)		(mm)	(mm)	(mm)
V5	2	2.5	4	10	20	Fig. 2a
V20	3.7	12	3	–	74	Fig. 2b
V45	3.7	12	3	–	166.5	Fig. 2b
H10	1	3.7	4	10	20	Fig. 2c
H30	1	3.7	3	–	30	Fig. 2d
H45	1	3.7	3	–	45	Fig. 2d
H80	1	3.7	3	–	80	Fig. 2d
H130	1	3.7	3	–	130	Fig. 2d

Fig. 2. Test configuration and specimen geometry for (a) four-point bending tests and (b) three-point bending tests with lay-up configuration (vertical build direction) and (c) four-point bending tests and (d) three-point bending tests with tilted configuration (horizontal build direction). The arrows point the lay-up directions. The red lines show the direction of the fibres in the visible surfaces. The tensile surface presents only 0° fibres (fibres aligned along the tensile stress direction) in case of lay-up configuration (a, b), and fifty-fifty 0/90° fibres in case of tilted configuration (c, d). (For interpretation of the references to colour in this figure legend, the reader is referred to the web version of this article.)

2.3. Modelling approach

The information obtained from the microstructural characterization was used to generate the Representative Volume Elements (RVEs) with varying fibre diameter and coating thickness to represent the variance in the analysed data. RVE was modelled and the orthotropic elastic properties of unidirectional composite were evaluated with the help of a commercial tool, MultiMechanics™ (Siemens Industry Software GmbH). Usually, RVEs exhibit an ideal microstructure with fixed packing or a microstructure with random values of input (such as fibre diameter) in a pre-defined range. The RVEs generated in current work, on the contrary, take the probability distribution function as input from the evaluated values obtained from microstructural characterization. A detailed study of the effects of RVE generation approach over the thermo-mechanical properties of UHTCMCs is an ongoing research and will be published in a future work. The microstructural features combined with the strength properties obtained from tests act as input for macroscale modelling in a commercial FEM software (ANSYS™ Workbench from ANSYS Inc). Solid shell elements were used to model the bending samples while keeping the number of layers and fibre orientation same as in the test samples. A damage initiation and damage evolution law were employed to determine the load limit of the samples. Maximum stress criterion was used for individual stress components as damage initiation criterion. For the evolution of damage, inbuilt instant stiffness reduction option

within ANSYS™ Workbench was used where the stiffness reduces by a pre-defined percentage after the satisfaction of the damage initiation criterion. In this way, the failure limit was determined for different test configurations with the help of progressive damage analysis. Other available criteria in ANSYS™ Workbench as damage initiation criterion are Puck, Hashin and Larc04, which are phenomenological in nature and can differentiate between failure modes. However, determination of parameters for these failure criteria through test, pose a massive challenge for this novel class of material. For example, the test required in determining the inclination parameters required for Puck failure criterion are well established for fibre reinforced polymer composites but there are no recommendations for CMC materials in the literature. However, it was necessary to figure out the stress component responsible for the failure of a sample under a particular test configuration with consideration of interaction of stress components. For this purpose, extended Tsai-Wu failure criterion proposed by Wim Van Paepegem [61] was implemented for a 3D finite element model to evaluate the direction dependent Tsai-Wu failure indices for each test configuration. These indices give a hint about the stress component majorly responsible for the failure of the bending sample. The failure surface in the stress space of the standard Tsai-Wu failure criterion can be given by [59]:

$$F_i\sigma_i + F_{ij}\sigma_i\sigma_j = 1 \tag{6}$$

where $i,j = 1,2,\cdots,6$; F_i and F_{ij} are strength tensors of the second and fourth rank, respectively. These values are the strength properties of a composite in different directions and $\sigma_{i,j}$ are stress components. With the introduction of safety ratio (R) and reformulation of the Eq. (6), the safety ratio can be obtained by solving the quadratic equation [62]:

$$(F_{ij}\sigma_i\sigma_j)R^2 + (F_i\sigma_i)R - 1 = 0 \tag{7}$$

By using R, the failure factor for any load case can be calculated. However, the original Tsai-Wu quadratic failure criteria do not differentiate between different failure modes. In 2003, Paepegem et al. [63] presented an extension of the Tsai-Wu failure criterion for progressive failure analysis. Instead of one failure index, a set of directional failure indices $\sum_{ij}$ were defined for the respective stress components σ_{ij} [63,64]. For example, the failure indices $\sum_{11}^{3D}$ can be calculated as shown in Eq. (8).

$$F_1\frac{\sigma_1}{\sum_{11}^{3D}} + F_2\sigma_2 + F_3\sigma_3 + F_{11}\left(\frac{\sigma_1}{\sum_{11}^{3D}}\right)^2 + F_{22}\sigma_2^2 + F_{33}\sigma_3^2$$
$$+ F_{44}\sigma_{13}^2 + F_{55}\sigma_{23}^2 + F_{66}\sigma_{12}^2 = 1 \tag{8}$$

The one-dimensional failure index $\sum_{ij}^{1D}$ is given by the ratio of σ_{ij} to the respective strength component. The relative importance of the failure index, $\sum_{11}$ was then calculated as in Eq. (9):

$$\sum_{11} = \frac{\sum_{11}^{3D}}{1 + (\sum_{11}^{3D} - \sum_{11}^{1D})} \tag{9}$$

In a similar fashion, the general Tsai-Wu quadratic criterion in stress space can be rewritten for the evaluation of $\sum_{22}$, $\sum_{33}$, $\sum_{12}$, $\sum_{23}$ and $\sum_{13}$ for the stress components σ_{22}, σ_{33}, σ_{12}, σ_{23}, and σ_{13}, respectively [43]. It is important to note here that the damage term used in the work of Paepegem was not considered in this paper, as it is out of scope of the current work. After the evaluation of these indices for a multiaxial stress state, a comparison of the indices can be made to find out stress components responsible for failure of the sample. These failure indices were evaluated with the help of a Python script and were then imported back to ANSYS™ Workbench to visualize the results.

3. Results and discussions

3.1. Microstructure

The investigated microstructural features are reported in Fig. 3 and Table 2. The obtained microstructure was characterized by a density of 1.82 g/cm³, which mainly reflected the high porosity of 27 vol% (except carbon fibre, all phases have a higher density: CVD carbon should have a density of 2.1–2.2 g/cm³ [65], PIP SiC of 3.2 g/cm³ [65], ZrB₂ and TaC of 6.1 [5] and 14.5 g/cm³ [6], respectively). The large porosity (visible as black holes in Fig. 3) is something which was expected and desired to fabricate a weak matrix composite characterized by higher toughness [66,67]. In fact, it is well known that seven impregnation steps are necessary to obtain open porosities below 10 vol% [68]. The final amount of UHTC was 4 vol% (bright particles in Fig. 3), which corresponded to a UHTC-to-SiC volumetric ratio of about 0.24. In the previous work [34], Uhlmann et al. showed trough EDX and XRD analysis that the bright particles are ZrB₂ (coarse particles up to 6 μm) or TaC (fine particles smaller than 1 μm). The fibre volumetric content, net of PyC coating, was 35 vol%. Polished section evidences the fibre distribution in the matrix in both directions perpendicular and parallel to the fibre and discloses a certain fibre disorder and misalignment.

Fig. 4 and Table 3 highlight further details of the obtained microstructure. The obtained median value of fibre diameter, and PyC fibre coating, was about 5.3 and 0.6 μm, respectively (Fig. 4a, b). The trend of the experimental CDF of diameter and fibre coating thickness attested the single-mode dispersion of the coated fibres in the consolidated composite. On the contrary, the fibre alignment was characterized by a bimodal distribution (Fig. 4c): about 71% of the fibres kept a misalignment within 1°, and the remaining 29% was centred at 5° of misalignment.

As for the matrix, since the ceramic is twice as dense as the polymer precursors, conventional PIP technique leads to the formation of cracks as a consequence of the large amount of shrinkage that accompanies hydrogen evolution and its transformation into the ceramic phase [73–76]. The shrinkage of SiC precursor led to the typical morphology obtained after PIP process [73–77]. The final network of cracks (Fig. 4d) produced blocks of SiC matrix characterized by a broad size distribution characterized by a median value of about 6 μm. Each block consisted in aggregated primary SiC particles of about 118 nm (Fig. 4e). It is noteworthy that the last pyrolysis cycle at 1600 °C did not convert all of the polymer in the third infiltration that appeared in the SEM micrographs as glassy layer over the aggregates (Fig. 4e).

3.2. Young's modulus

As showed in Fig. 5a, the measured Young's modulus of 56 ± 6 GPa agrees with the expected one calculated using the measured microstructural features and the moduli of the constituent phases (Table 4). The calculated Young's modulus of the composite (E_c) was estimated by integrating the observed distribution of the fibre misalignment (Σ_θ) into the classical laminate theory [78]:

$$\frac{1}{E_c(\theta)} = \frac{\cos^4(\theta)}{E_{c,1}} + \frac{\sin^4(\theta)}{E_{c,2}} + \left(\frac{1}{G_{c,12}} - \frac{2v_{c,12}}{E_{c,1}}\right) \cos^2(\theta) \sin^2(\theta) \tag{10}$$
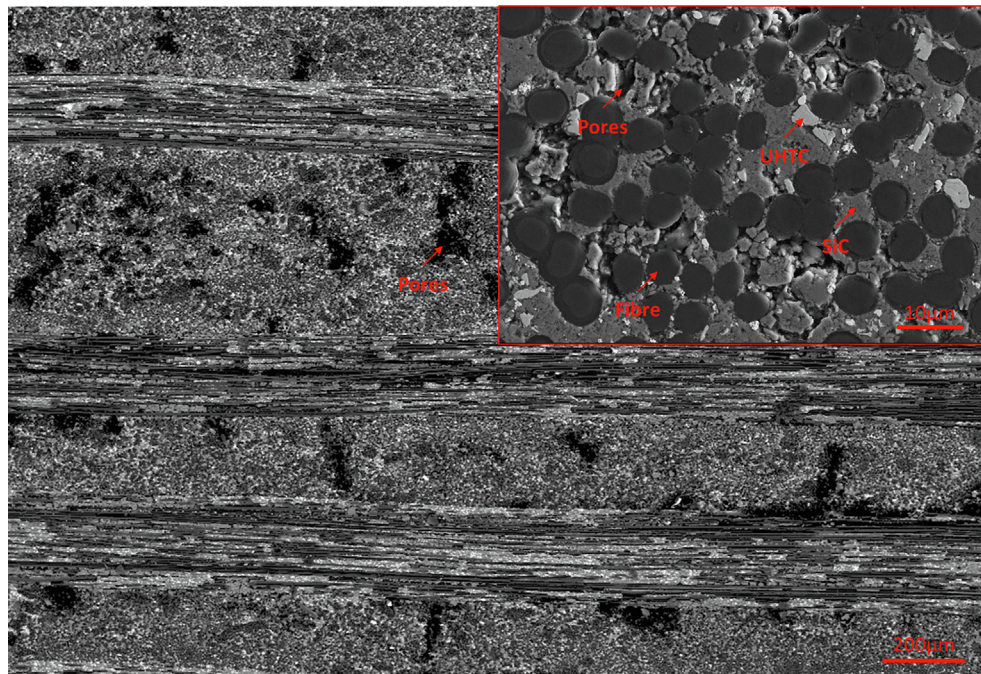

Fig. 3. SEM micrograph of the polished cross section of the unwound C$_f$/SiC composites enriched of ZrB₂ and TaC (Z50 specimen) with high magnification image inset. The arrows point the presence of dispersed UHTC grains (light grey), SiC matrix (medium grey), Toray T800 PAN fibre (dark grey), and pores (black area).

Table 2

Microstructural and mechanical properties of unwound C_f/SiC composites enriched of ZrB_2 and TaC UHTC (labelled as Z50) and EADS - Astrium's C_f/SiC material named SICARBON™ [68–71]. ρ: density. P: porosity. V_f: fibre volumetric content. ILSS: interlaminar shear strength.

	ρ (g/cm³)	P (%)	SiC (%)	UHTC (%)	V_f (%)	PyC (%)	E_c (GPa)	$σ_t$ (MPa)	$σ_f$ (MPa)	ILSS (MPa)
Z50	1.82	27 ± 2	17 ± 2	4 ± 1	35 ± 3	17 ± 2	56 ± 6	–	370 ± 15[a]	4.0 ± 0.4
SICARBON™	1.8	22[c] (8)	24[c]	0	37[b]	19[b]	85 ± 5	365 ± 105	500	15 ± 5

[a] Mean value obtained with all the H-specimens fractured through 3-point bending.

[b] Measured through image analysis on Fig. 5d of Ref. [72] and by taking into account the fibre diameter to coating thickness ratio reported in Fig. 4a, b.

[c] Calculated by considering the density of the composite (1.8 g/cm³), the theoretical density of SiC (3.2 g/cm³), and the volumetric content of fibre (37%) and coating (19%).
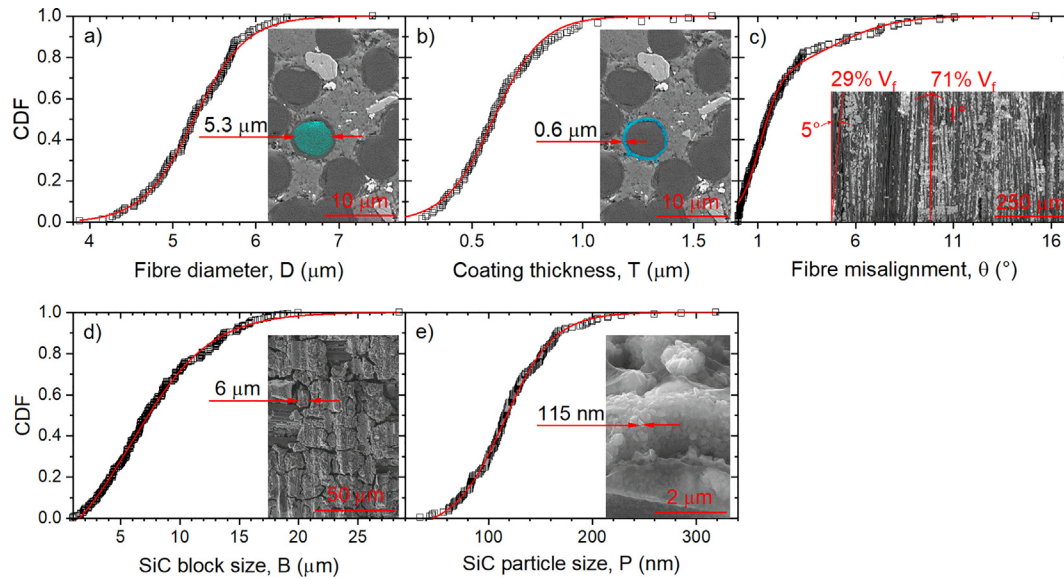

Fig. 4. Cumulative distribution function, CDF, of (a) equivalent fibre diameter, D, (b) thickness of fibre coating, T, (c) fibre misalignment, θ, (d) size of SiC aggregate, B, and (e) particle size of SiC, P. The sigmoidal trend of measured values (open square symbols) was fitted with modified Boltzmann function (solid red line, R² > 0.99). (For interpretation of the references to colour in this figure legend, the reader is referred to the web version of this article.)

Table 3

Parameters of fitted CDFs according to Eq. (1).

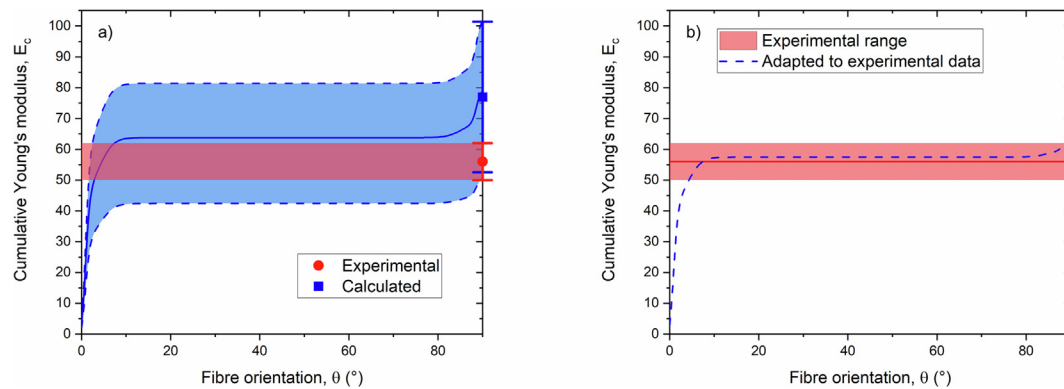| x	p_1	x_1	a_1	b_1	x_2	a_2	b_2
D (µm)	1	5.25794	0.31091	−2	0	1	0
T (µm)	1	0.59682	0.10965	−2	0	1	0
θ (°)	0.71493	1.11597	−0.54086	0	4.85818	−1.55956	−1
B (µm)	1	5.9636	3.28882	−2.25876	0	1	0
P (nm)	1	118.11211	22.02992	−2	0	1	0

Fig. 5. Experimental Young's modulus measured through the resonance frequency method and predicted cumulative Young's modulus vs. content of the fibres sorted as function of their orientation (Eq. (11)). In (a) the prediction is based, in one case, on the maximum values reported in Table 4 (upper limit), in the other on the minimum values (lower limit). The solid curve is the average of these two limit cases. As for the prediction in (b) were taken only the maximum values of the fibre properties and the minimum values of the matrix properties.

Table 4

Range of elastic properties values of the single phases and a unidirectional lamina (the last four rows). The micromechanics models refer to the rule of mixtures and the inverse rule of mixtures.

Elastic property	Symbol	Range (GPa)			Ref.
Longitudinal modulus of the fibre	$E_{f,1}$	235	-	294	From Ref. [80,81]
Transverse modulus of the fibre	$E_{f,2}$	10	–	20	From Ref. [82]
In-plane shear modulus of the fibre	$G_{f,12}$	2	–	27	From Ref. [80,83]
Major Poisson's ratio of the fibre	$v_{f,12}$	0.24	–	0.28	From Ref. [81,84]
Young's modulus of PyC	E_{PyC}	12	–	26	From Ref. [85]
Shear modulus of PyC	G_{PyC}	2	–	10	From Ref. [85]
Young's modulus of SiC	E_{SiC}	155	–	420	From Ref. [86,87]
Shear modulus of SiC	G_{SiC}	160	–	227	From Ref. [88]
Young's modulus of UHTC	E_{UHTC}	340	–	540	From Ref. [6]
Shear modulus of UHTC	G_{UHTC}	177	–	246	From Ref. [88]
Young's modulus of the matrix	E_m	22	–	110	Calculated in agreement with Ref. [86,89]
Shear modulus of the matrix	G_m	10	–	50	
Poisson's ratio of the matrix	v_m	0.10	–	0.15	
			–		
Longitudinal modulus of a composite ply	$E_{c,1}$	90	–	180	Calculated by using simple micromechanics models [79]
Transverse modulus of a composite ply	$E_{c,2}$	16	–	41	
Shear modulus of a composite ply	$G_{c,12}$	4	–	38	
Major Poisson's ratio of a composite ply	$v_{c,12}$	0.15	–	0.20	

$$E_c = \int_{0°}^{90°} \left(\frac{d\Sigma_\theta}{d\theta} \cdot E_c(\theta) \right) d\theta \qquad (11)$$

where the orientation dependence of the elastic modulus ($E_c(\theta)$) of a unidirectinal lamina without fibre misalignment is a function of its longitudinal and transverse moduli ($E_{c,1}$ and $E_{c,2}$, respectively), in-plane shear modulus ($G_{c,12}$) and major Poisson ratio ($v_{c,12}$). Eq. (11) plotted in Fig. 5a shows the contributions of the layers at 0° and 90° onto the overall Young's modulus, as demonstrated by the two-step increase of the cumulative Young's modulus close to 0° and 90°. The increase is not net at these two angles because of the distribution of fibre misalignment. The calculated contribution of the transverse layer is in the range of 10–20 %. The calculated range is most affected by the uncertainty on E_m that needs refinement. However, the trend is anyway consistent with the experimental results and confirms the microstructural analysis. It is worth to note that the resonance method is not a standard technique for fibre-reinforced composite characterized by a porous matrix and may lead to underestimation of the elastic modulus due to scattering of acoustic waves at interfaces/porosity. This consideration may be consistent with the reason why the experimental values fall near the calculated lower limit. On the other side, if we try to fix the calculated value, the smallest difference with respect to the measured values was found by using the maximum values related to the fibre and the minimum values related to the matrix (Fig. 5b). Hence, according to this approach the matrix should have a Young's modulus of 22 GPa that could be consistent with the large content of porosity and PyC.

3.3. Interlaminar shear strength

All the specimens tested with vertical build direction exhibited shear failure near their mid-thickness and in the form of longitudinal cracks (Fig. 6a, b). The other delamination cracks, closer to the outer surfaces of the specimens, developed later. All the delamination cracks mainly developed along the interface between longitudinal and transverse plies, as it can be seen in Fig. 6a–c. As commonly observed in carbon fibre-reinforced composites [89], this could be due to the concentration of residual thermal stress between the adjacent plies with different fibre orientation. The recorded stress-strain curves (Fig. 7a) show the typical trend of interlaminar failure [90]: the stress drop after the nominal maximum stress is followed by a load increase (samples V20 and V45). The different trend showed by V5 samples should be ascribed

to the occurring of local damage under the loading cylinders. As expected for the tests, which failed under interlaminar shear, no plateau was observed and apparent ILSS showed a decreasing trend as the s/t ratio was increased (Fig. 7b). This same trend was reported in other experimental investigations as well [52]. The low value of ILSS should be ascribed mainly to the large number of pores and cracks spread within the matrix (i.e. low matrix densification) and voids (i.e. open porosities due to the few impregnation steps) that cut down the bond between the stacked plies. On the other hand, the nominal maximum stress achieved in the tensile surface linearly increased up to 365 ± 15 MPa at s/t = 45 (Fig. 7). As recommended by ASTM C1341 – 13 standard for composites with low ILSS (<3.5 MPa) based on low matrix density or shear failure at interfaces, a s/t ratio of 60 should be used to prevent shear failures.

3.4. Flexural strength

Flexure type failure was imposed by machining the specimens with different ply orientation: from vertical build direction to horizontal build direction (Fig. 2c, d). With this configuration, all the tested specimens showed a tensile failure under the bending moment (Fig. 6d, e show the tensile surface after test). No failure due to interlaminar shear stress was observed, not even at the low s/t ratio of 10. However, an invalid test was produced at s/t = 10 due to in-plane shear failure. The appearing of in-plane shear failure at low s/t ratio was favoured by the small thickness of the samples (1 mm) and confirmed that the stacking surfaces are critical in such composites. In Fig. 6d, the plies with fibre at 90° with respect to the applied tensile stress showed a multiple splitting failure. On the other hand, the plies with fibre aligned to the applied tensile stress direction showed a fibre bridging even at the maximum crack opening displacement. This evidence suggests that only the 0° layers withstood the load up to the nominal maximum stress, while the 90° layers cracked several times as the stress sustained by the 0° layers increased. Higher-magnification SEM observations of the fracture surface (Fig. 6f) revealed matrix particulates remaining adhered to the surface of pulled out fibres. This result suggests that no debonding at C/C interface (fibre/coating interface) occurred. Failure involved debonding of matrix/coating interface or by cracking the matrix, which remained bonded to the coating of the pulled-out fibre. This observation attests to the efficacy of the matrix in mitigating stress concentrations around fibre and hence yielding matrix weak composite behaviour, i.e.
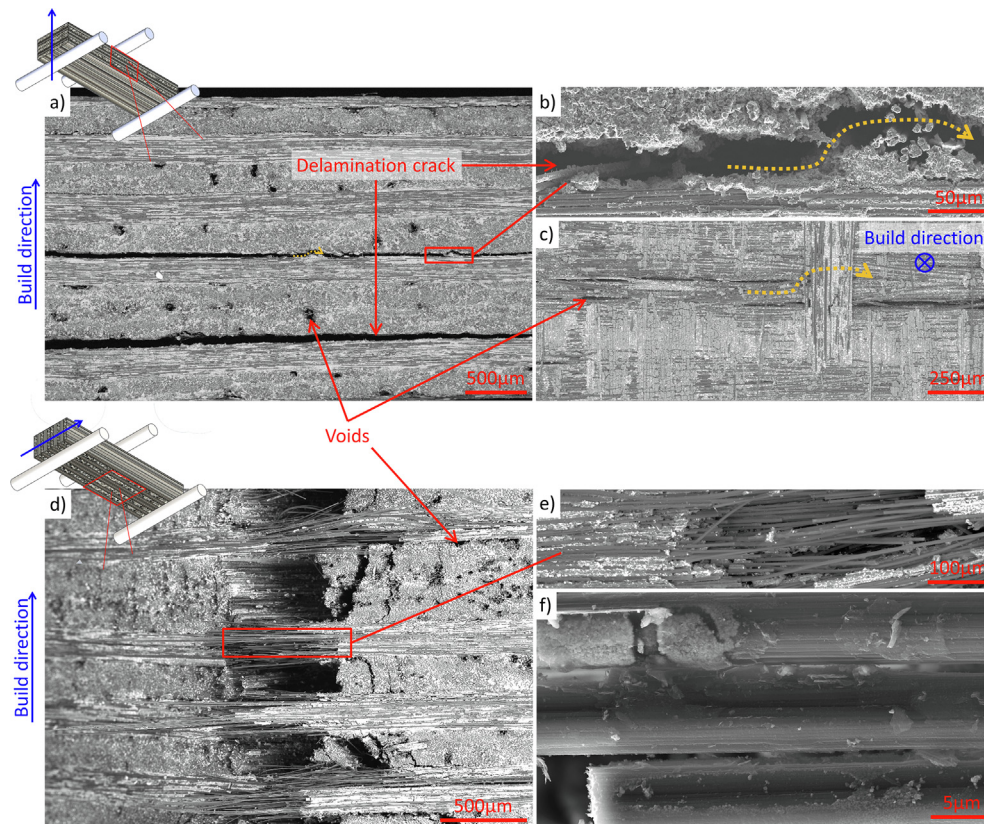
Fig. 6. SEM micrograph of composite with lay-up configuration (vertical build direction) failed under interlaminar shear stress produced by bending test: (a, b) lateral view and (c) delaminated surface. Dotted arrows highlight crack deflection. (d, e) Tensile surface of composite tested with tilted configuration (horizontal build direction) showing tensile failure under the bending moment. (f) Pulled-out fibres.

damage tolerant behaviour [67]. The recorded stress-strain curves (Fig. 7a) show a constant decrease in stress after maximum point. These non-catastrophic failures, sometime also called fibrous or graceful failures, were observed up to s/t ratio of 30 (H10 and H30 samples). Further increasing s/t, owing to the proportional increasing of the deflection at beam centre at maximum applied force, the larger strain energy release rate produced a catastrophic failure. Only for the H45 specimens, the load then dropped to a residual value, which was about 30% of the peak load. For all the H45, H80 and H130 specimens, at the ultimate point of the test, the two broken pieces flew away. Ultimate damage mechanisms aside, the valid flexural failure made it possible to measure the flexural strength. The goodness of the measurement is attested by the invariance with respect to the s/t ratio (Fig. 7b). Hence the flexural strength of these composites is 370 ± 20 MPa. Moreover, according to the above failure analysis and the Hart-Smith 10% rule, the 0° layers withstood a maximum tensile stress of 670 MPa and an ultimate strain of 1%. PLS_{max} was 280 MPa (510 MPa if 10% rule is considered). The decrease of stiffness after PLS_{max} should be ascribed to the failure onset of 0° layers and/or crack onset by in plane shear stress, rather than failure of 90° layers. In fact, since the loss of linearity was calculated starting from about 0.3% of strain (the point where the maximum slope was achieved), the failure of 90° layers did not contribute to the calculated linearity loss of 5%, because they should have failed before between 4 and 20 MPa [44]. As expected in a weak matrix composite [91], after matrix-cracking, the damage evolution should be dominated by the fibres. From the failure onset of on-axis layers (PLS_{max}) to their final failure (σ_f), the observed nonlinear behaviour may be attributed to better alignment of the fibres, allowed by the coating and the high porosity of the matrix, to the tensile stress.

3.5. Modelling

In Tables 5 and 6, the mechanical properties used in the current analysis are shown. The values of elastic properties (Table 5) of fibre and coating and matrix were taken from the literature [80,82] while assuming the presence of high porosity degraded mechanical properties of the matrix [89]. It should be noted that the Young's modulus of the fibre was taken as 235 GPa instead of 294 GPa, as mentioned in the data sheet from the manufacturer and observed in this work to match the calculated value of the composite to the experimental one (Fig. 5b). Since the other elastic properties of the fibre were taken from a dataset reported in the literature, for the sake of consistency, Young's modulus was also taken from the same reference. The resulting Young's moduli used for homogenization of the uni-directional Z50 composite (Table 5) fall near the calculated lower limits reported in Table 4. The tensile strength properties of unidirectional layers were taken from the bending tests performed within the framework of current work. The strength properties under compression and shear were taken from the test campaign of the EU project C^3harme [23]. The homogenized elastic properties (Table 5) of the composites were then evaluated after applying planar boundary conditions on the surface of the 3D RVE in MultiMechanics™.

The properties from Tables 5 and 6 were then used an input for ANSYS™ Workbench. The stiffness of the elements was reduced by 5%, derived from the measured change in linearity in the force–displacement curves of the tested samples. A displacement load was applied on all the samples in 10 sub steps. After reaching the defined strength limit, the stiffness reduces to 95% of the original value and is carried on to the next loading step. In Fig. 8, the virtual force displacement curves of all three-point bending samples are shown together with the corresponding experimental curves. A
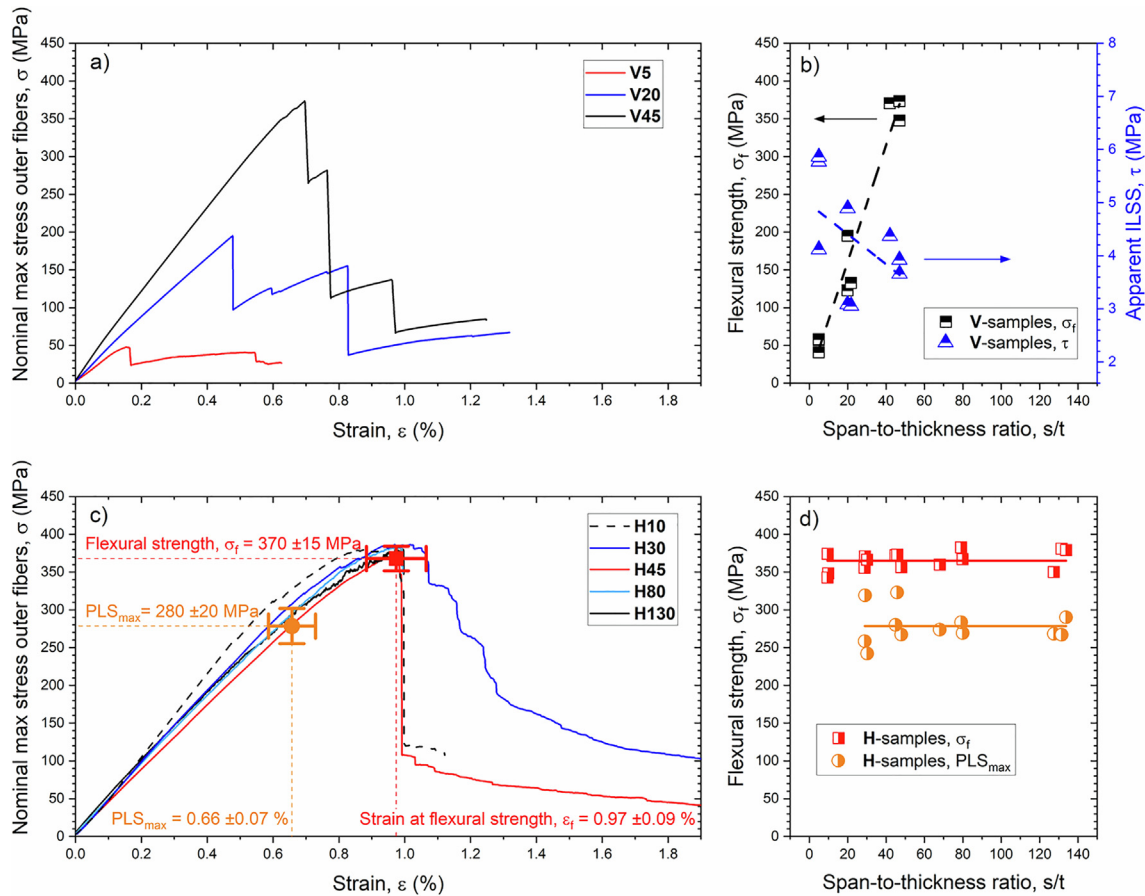
Fig. 7. (a) Flexural stress vs. strain curves and (b) flexural strength (half up squares) and apparent interlaminar shear strength (half up triangles) vs. span-to-thickness ratio of specimens with lay-up configuration. (c) Flexural stress vs. strain curves and (d) flexural strength (half right squares) and maximum proportional limit stress (PLS$_{max}$, half right circles) vs. span-to-thickness ratio of specimens with tilted configuration. In (c) the red square and the orange circle represent the mean value of the flexural strength and PLS$_{max}$, respectively, of all the H-specimens fractured through 3-point bending. (For interpretation of the references to colour in this figure legend, the reader is referred to the web version of this article.)

Table 5
Elastic properties of the constituent (fibre, fibre coating and matrix) used for homogenization and that of the resulting uni-directional composite (Z50).

	E_1 (GPa)	E_2 (GPa)	E_3 (GPa)	v_{12} (-)	v_{13} (-)	v_{23} (-)	G_{12} (GPa)	G_{13} (GPa)	G_{23} (GPa)
Fibre	235	14	14	0.24	0.24	0.1	11	11	10
Coating	12	20	20	0.25	0.25	0.25	5	5	5
Matrix	20	20	20	0.14	0.14	0.14	–	–	–
Z50	75	17	17	0.19	0.19	0.18	7	7	7

Table 6
Strength properties obtained from the bending tests for a layer with 0° orientation. Superscripts T and C refers to tension and compression, respectively.

	σ_1^T (MPa)	$\sigma_2^T = \sigma_3^T$ (MPa)	σ_1^C (MPa)	$\sigma_2^C = \sigma_3^C$ (MPa)	$\sigma_{12} = \sigma_{13}$ (MPa)	σ_{23} (MPa)
Z50	670	25	504	100	21	4

good agreement of the values obtained from the progressive damage model was found in prediction of the load limit of the samples.

The stress state obtained at the displacement limit was used for the evaluation of direction dependent Tsai-Wu failure indices. The equations from Section 2.3 were used in evaluation of Tsai-Wu failure indices for the samples in the local fibre coordinate system (1: fibre, 2: in-plane transverse, 3: out-of plane transverse). It was observed, as shown in Fig. 9, that V-samples fail mainly due to interlaminar shear stress as implied by the presence of higher percentage of Σ_{23}. However, as s/t ratio is increased from 20 to 45 in V-

samples, the contribution of Σ_{11} and Σ_{22} increases but Σ_{23} remains the major contributor when compared to other failure indices. On the other hand, all the H-samples fail majorly due to Σ_{11} and Σ_{22}.

This comparison becomes clear in the Fig. 10 where the finite element results from V45 and H45 are shown. In sample V45, the outermost layers fail due to σ_{11} (red) since they are oriented in 0° followed by 90° layers which fail due to σ_{22} (orange) in the mid-section (Fig. 10a). The delamination due to interlaminar shear starts from the area close to the neutral axis and it increases as one move away from the mid-section towards either side (Fig. 10b) of
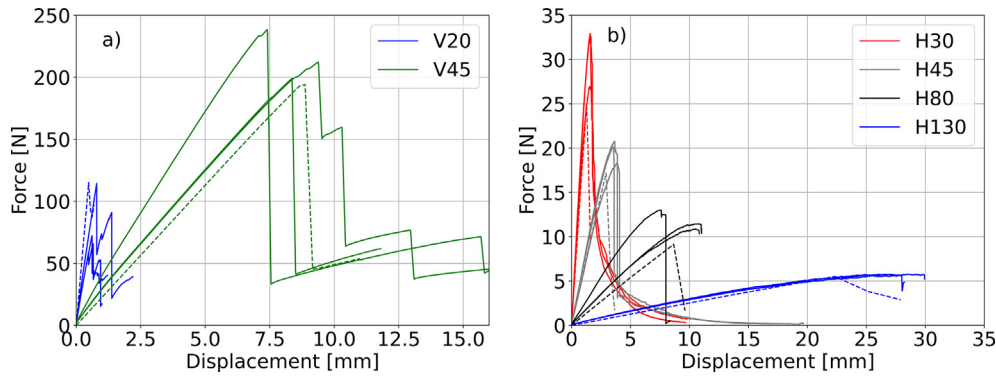
Fig. 8. Force displacement curves obtained from the tests (solid lines) and the curve obtained from finite element simulation (broken line) for (a) vertical and (b) horizontal test configuration.
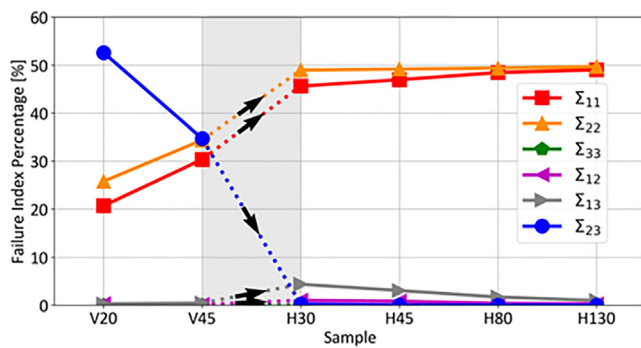

Fig. 9. Percentage of failure indices of elements in the finite element model for different samples where Σ_{ij} represents the contribution of respective stress component σ_{ij}. 'V' and 'H' on x-axis denote the 'vertical' and 'horizontal' build up respectively with varying s/t ratio.

the sample. On the contrary, H45 exhibits failure mostly due to σ_{11} and σ_{22} except for some elements which fail due to in-plane shear in the mid-section (Fig. 10c) on the tensile side of the flexural sample. When H45 is compared with other H-samples with higher s/t

ratios, as observed in Fig. 9, only a minor increase in Σ_{11} and Σ_{22} is observed which demonstrates the size independency of H-samples in producing valid flexural results with *iso*-strain conditions in both 0° and 90° layers.

3.6. Benchmark against SICARBON™

The critical tensile stress of Z50 samples, measured by applying a flexural moment, matches well with the tensile strength measured on SICARBON™ through tensile tests (Table 2). This is expected, since both the composites had the same fibre volumetric content, the stacked layers in both tests (flexural test of Z50 with horizontal build direction, and tensile test of SICARBON™) had the same fibre orientation with respect to the applied maximum tensile stress (fifty-fifty 0/90° fibres) and the maximum tensile stress was borne by fibres rather than cracked matrices characterized by low density. Hence, the UHTC enrichment of 24% (4 vol% of UHTC on 17 vol% of SiC) did not affect the tensile strength of SICAR-BON™. On the other hand, the higher σ_f of SICARBON™ should be due the different bending configurations: most likely, lay-up configuration with 100% of 0° fibres in the tensile surface and s/t larger than 45. Unfortunately, the experimental set-up is not reported in
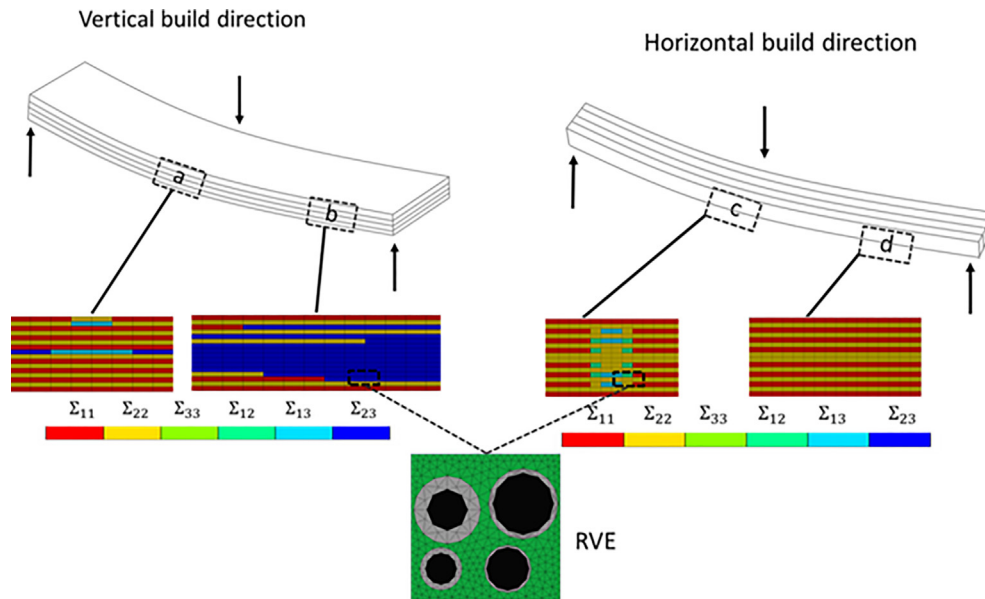

Fig. 10. Finite element results of the cross section of samples (a-d) with [0/90]$_{4S}$ layup with vertical build direction and horizontal build direction where the elastic constants are evaluated from RVE. The size of RVE is 18.2 μm × 18.2 μm × 18.2 μm.

literature. For the same reason, above all the ILSS cannot be compared because it is strongly affected by the test configuration. However, the above flexural tests confirmed that surfaces between two stacked layers are critical and showed a low interlaminar shear strength. Finally, we want to point out that the declared porosity value reported in literature of SICARBON™ of 8% is not the total porosity, but only the open porosity that does not consider the cracks of the matrix produced by the polymer shrinkage, and the voids inside the composite. Hence, in our opinion the two compared materials had similar microstructures in terms of matrix relative density and fibre volumetric content and showed comparable mechanical strength even when about one fifth of the SiC was replaced with UHTC.

4. Conclusions

The microstructure of SICARBON™ enriched with 4 vol% of UHTC was extensively characterized trough image analysis. The measured volume contents of the constitutive phases and the extracted cumulative distribution function of the characterising microstructural features were reported, respectively, as single values and as parameters of an appropriately modified Boltzmann function. In this way, the reported microstructural framework offers a sort of microstructural genome that can be easily integrated in the models. The goodness of the measured microstructural features was checked by comparing the output of the analytical modelling of the Young's modulus with the measured value. This comparison agreed with the low density of the UHTC-enriched CMC (1.82 g/cm^3) and the large porosity amount (27 vol%) and suggested that the matrix should have a Young's modulus of about 20 GPa. As expected, the weak matrix resulted in a low ILSS (4 MPa) that caused the shear failure even at s/t = 45. On the other hand, specimens tested with tilted configuration gave valid flexural failure under tensile stress throughout the large s/t range, from 10 to 130. Hence, this configuration can be exploited to obtain valid flexural strength while utilizing small quantity of plate material very efficiently. The flexural strength of 370 MPa is comparable to that of the already well-developed SICARBON™ product: 4 vol% of UHTC enrichment did not actually affect the flexural strength. Finally, a finite element model was developed and the results were in agreement with the experimentally observed failure behaviour. With the help of directional dependent failure indices, test configurations can be optimized in the future for determination of valid properties of CMCs.

Acknowledgement

References

[1] N.P. Padture, Advanced structural ceramics in aerospace propulsion, Nat. Mater. 15 (2016) 804–809, https://doi.org/10.1038/nmat4687.

[2] X.W. Yin, L.F. Cheng, L.T. Zhang, N. Travitzky, P. Greil, Fibre-reinforced multifunctional SiC matrix composite materials, Int. Mater. Rev. 62 (2017) 117–172, https://doi.org/10.1080/09506608.2016.1213939.

[3] F. Süß, T. Schneider, M. Frieß, R. Jemmali, F. Vogel, L. Klopsch, D. Koch, Combination of PIP and LSI processes for SiC/SiC ceramic matrix composites, Open Ceram. 5 (2021), https://doi.org/10.1016/j.oceram.2021.100056 100056.

[4] T.A. Jackson, D.R. Eklund, A.J. Fink, High speed propulsion: performance advantage of advanced materials, J. Mater. Sci. (2004) 5905–5913, https://doi.org/10.1023/B:JMSC.0000041687.37448.06.

[5] W.G. Fahrenholtz, G.E. Hilmas, I.G. Talmy, J.A. Zaykoski, Refractory Diborides of Zirconium and Hafnium, J. Am. Ceram. Soc. 90 (2007) 1347–1364, https://doi.org/10.1111/j.1551-2916.2007.01583.x.

[6] B. Raju Golla, A. Mukhopadhyay, B. Basu, S. Kumar Thimmappa, Review on ultra high temperature boride ceramics, Prog. Mater. Sci. (2020), https://doi.org/10.1016/j.pmatsci.2020.100651 100651.

[7] E.P. Simonenko, N.P. Simonenko, V.G. Sevastyanov, N.T. Kuznetsov, ZrB2/HfB2–SiC ceramics modified by refractory carbides: an overview, Russ. J. Inorg. Chem. 64 (2019) 1697–1725, https://doi.org/10.1134/S0036023619140079.

[8] L. Silvestroni, C. Melandri, V. Venkatachalam, J. Binner, D. Sciti, Merging toughness and oxidation resistance in a light ZrB2 composite, Mater. Des. 183 (2019), https://doi.org/10.1016/j.matdes.2019.108078 108078.

[9] L. Silvestroni, S. Failla, N. Gilli, C. Melandri, U. Savacı, S. Turan, D. Sciti, Disclosing small scale length properties in core-shell structured B4C-TiB2 composites, Mater. Des. 197 (2021), https://doi.org/10.1016/j.matdes.2020.109204 109204.

[10] Q. Feng, P. Lin, G. Ma, T. Lin, P. He, W. Long, Q. Zhang, Design of multi-layered architecture in dissimilar ceramic/metal joints with reinforcements clustering away from both substrates, Mater. Des. 198 (2021), https://doi.org/10.1016/j.matdes.2020.109379 109379.

[11] G.M. Song, Y. Zhou, S.J.L. Kang, Experimental description of thermomechanical properties of carbon fiber-reinforced TiC matrix composites, Mater. Des. 24 (2003) 639–646, https://doi.org/10.1016/S0261-3069(03)00124-9.

[12] C. Ma, L. Guo, H. Li, W. Tan, T. Duan, N. Liu, M. Zhang, Effects of high-temperature annealing on the microstructures and mechanical properties of C/C-ZrC-SiC composites prepared by precursor infiltration and pyrolysis, Mater. Des. 90 (2016) 373–378, https://doi.org/10.1016/j.matdes.2015.10.140.

[13] M. yan Zhang, K. zhi Li, X. hong Shi, W. long Tan, Effects of SiC interphase on the mechanical and ablation properties of C/C-ZrC-ZrB2-SiC composites prepared by precursor infiltration and pyrolysis, Mater. Des. 122 (2017) 322–329. https://doi.org/10.1016/j.matdes.2017.02.086.

[14] D. Sciti, L. Zoli, L. Silvestroni, A. Cecere, G.D. Di Martino, R. Savino, Design, fabrication and high velocity oxy-fuel torch tests of a Cf-ZrB2 - fiber nozzle to evaluate its potential in rocket motors, Mater. Des. 109 (2016) 709–717, https://doi.org/10.1016/j.matdes.2016.07.090.

[15] J. Binner, M. Porter, B. Baker, J. Zou, V. Venkatachalam, V.R. Diaz, A. D'Angio, P. Ramanujam, T. Zhang, T.S.R.C. Murthy, Selection, processing, properties and applications of ultra-high temperature ceramic matrix composites, UHTCMCs – a review, Int. Mater. Rev. (2019) 1–56, https://doi.org/10.1080/09506608.2019.1652006.

[16] D. Zhang, P. Hu, S. Dong, X. Liu, C. Wang, Z. Zhang, X. Zhang, Oxidation behavior and ablation mechanism of Cf/ZrB2-SiC composite fabricated by vibration-assisted slurry impregnation combined with low-temperature hot pressing, Corros. Sci. 161 (2019), https://doi.org/10.1016/j.corsci.2019.108181.

[17] H. Ouyang, Y. Zhang, C. Li, G. Li, J. Huang, H. Li, Effects of ZrC/SiC ratios on mechanical and ablation behavior of C/C–ZrC–SiC composites prepared by carbothermal reaction of hydrothermal co-deposited oxides, Corros. Sci. 163 (2019), https://doi.org/10.1016/j.corsci.2019.108239 108239.

[18] L.M. Rueschhoff, C.M. Carney, Z.D. Apostolov, M.K. Cinibulk, Processing of fiber-reinforced ultra-high temperature ceramic composites: a review, Int. J. Ceram. Eng. Sci. 2 (2020) 22–37, https://doi.org/10.1002/ces2.10033.

[19] X. Luan, G. Liu, M. Tian, Z. Chen, L. Cheng, Damage behavior of atomic oxygen on a hafnium carbide-modified C/SiC composite, Compos. Part B Eng. (2021), https://doi.org/10.1016/j.compositesb.2021.108888 108888.

[20] H. Ouyang, G. Li, C. Li, J. Huang, J. Fei, J. Lu, Microstructure and ablation properties of C/C-Zr-Si-O composites prepared by carbothermal reduction of hydrothermal co-deposited oxides, Mater. Des. 159 (2018) 145–154, https://doi.org/10.1016/j.matdes.2018.08.048.

[21] Y. Jia, X. Yao, J. Sun, H. Li, Effect of ZrC particle size on the ablation resistance of C/C-ZrC-SiC composites, Mater. Des. 129 (2017) 15–25, https://doi.org/10.1016/j.matdes.2017.05.019.

[22] S. Chen, C. Zhang, Y. Zhang, H. Hu, Influence of pyrocarbon amount in C/C preform on the microstructure and properties of C/ZrC composites prepared via reactive melt infiltration, Mater. Des. 58 (2014) 570–576, https://doi.org/10.1016/j.matdes.2013.12.071.

[23] c3harme (n.d.). https://c3harme.eu/ (accessed September 10, 2019).

[24] L. Zoli, A. Vinci, P. Galizia, C. Melandri, D. Sciti, On the thermal shock resistance and mechanical properties of novel unidirectional UHTCMCs for extreme environments, Sci. Rep. 8 (2018) 9148, https://doi.org/10.1038/s41598-018-27328-x.

[25] P. Galizia, S. Failla, L. Zoli, D. Sciti, Tough salami-inspired Cf/ZrB2 UHTCMCs produced by electrophoretic deposition, J. Eur. Ceram. Soc. 38 (2018) 403–409, https://doi.org/10.1016/j.jeurceramsoc.2017.09.047.

[26] S. Failla, P. Galizia, L. Zoli, A. Vinci, D. Sciti, Toughening effect of non-periodic fiber distribution on crack propagation energy of UHTC composites, J. Alloys Compd. 777 (2019) 612–618, https://doi.org/10.1016/J.JALLCOM.2018.11.043.

[27] Y. Liu, Y. Zu, H. Tian, J. Dai, J. Sha, Microstructure and mechanical properties of continuous carbon fiber-reinforced ZrB2-based composites via combined electrophoretic deposition and sintering, J. Eur. Ceram. Soc. 41 (2021) 1779–1787, https://doi.org/10.1016/j.jeurceramsoc.2020.10.044.

[28] D. Zhang, P. Hu, J. Feng, M. Xie, H. Zhao, X. Zhang, Characterization and mechanical properties of C f/ZrB 2 -SiC composites fabricated by a hybrid technique based on slurry impregnation, polymer infiltration and pyrolysis and low-temperature hot pressing, Ceram. Int. 45 (2019) 5467–5474, https://doi.org/10.1016/j.ceramint.2018.12.001.

[29] D. Zhang, P. Hu, S. Dong, S. Qu, X. Zhang, Effect of pyrolytic carbon coating on the microstructure and fracture behavior of the Cf/ZrB2-SiC composite, Ceram. Int. 44 (2018) 19612–19618, https://doi.org/10.1016/J.CERAMINT.2018.07.210.

[30] C. Fang, P. Hu, S. Dong, P. Xie, K. Wang, X. Zhang, Design and optimization of the coating thickness on chopped carbon fibers and sintering temperature for ZrB 2 -SiC-C f composites prepared by hot pressing, J. Eur. Ceram. Soc. 39 (2019) 2805–2811, https://doi.org/10.1016/j.jeurceramsoc.2019.03.038.

[31] D. Sciti, L. Zoli, A. Vinci, L. Silvestroni, S. Mungiguerra, P. Galizia, Effect of PAN-based and pitch-based carbon fibres on microstructure and properties of continuous Cf/ZrB2-SiC UHTCMCs, J. Eur. Ceram. Soc. 41 (2020) 3045–3050, https://doi.org/10.1016/j.jeurceramsoc.2020.05.032.

[32] S. Chen, Y. Zhang, C. Zhang, D. Zhao, H. Hu, Z. Zhang, Effects of SiC interphase by chemical vapor deposition on the properties of C/ZrC composite prepared via precursor infiltration and pyrolysis route, Mater. Des. 46 (2013) 497–502, https://doi.org/10.1016/j.matdes.2012.09.019.

[33] S. Chen, H. Hu, Y. Zhang, C. Zhang, Q. Wang, Effects of TaC amount on the properties of 2D C/SiC-TaC composites prepared via precursor infiltration and pyrolysis, Mater. Des. 51 (2013) 19–24, https://doi.org/10.1016/j.matdes.2013.03.073.

[34] F. Uhlmann, C. Wilhelmi, S. Schmidt-Wimmer, S. Beyer, C. Badini, E. Padovano, Preparation and characterization of ZrB2 and TaC containing Cf/SiC composites via Polymer-Infiltration-Pyrolysis process, J. Eur. Ceram. Soc. 37 (2017) 1955–1960, https://doi.org/10.1016/j.jeurceramsoc.2016.12.048.

[35] H. Hu, Q. Wang, Z. Chen, C. Zhang, Y. Zhang, J. Wang, Preparation and characterization of C/SiC–ZrB2 composites by precursor infiltration and pyrolysis process, Ceram. Int. 36 (2010) 1011–1016, https://doi.org/10.1016/j.ceramint.2009.11.015.

[36] S. Chen, C. Zhang, Y. Zhang, H. Hu, Preparation and properties of carbon fiber reinforced ZrC–ZrB2 based composites via reactive melt infiltration, Composites Part B 60 (2014) 222–226, https://doi.org/10.1016/j.compositesb.2013.12.067.

[37] D. Zhao, C. Zhang, H. Hu, Y. Zhang, Preparation and characterization of three-dimensional carbon fiber reinforced zirconium carbide composite by precursor infiltration and pyrolysis process, Ceram. Int. 37 (2011) 2089–2093, https://doi.org/10.1016/j.ceramint.2011.02.024.

[38] S. Chen, C. Zhang, Y. Zhang, D. Zhao, H. Hu, X. Xiong, Effects of polymer derived SiC interphase on the properties of C/ZrC composites, Mater. Des. 58 (2014) 102–107, https://doi.org/10.1016/j.matdes.2014.01.039.

[39] S. Tang, J. Deng, S. Wang, W. Liu, K. Yang, Ablation behaviors of ultra-high temperature ceramic composites, Mater. Sci. Eng. A 465 (2007) 1–7, https://doi.org/10.1016/j.msea.2007.02.040.

[40] A. Paul, V. Rubio, J. Binner, B. Vaidhyanathan, A. Heaton, P. Brown, Evaluation of the high temperature performance of HfB2 UHTC particulate filled Cf/C composites, Int. J. Appl. Ceram. Technol. 14 (2017) 344–353, https://doi.org/10.1111/ijac.12659.

[41] Z. Wang, S. Dong, X. Zhang, H. Zhou, D. Wu, Q. Zhou, D. Jiang, Fabrication and properties of C f/SiC-ZrC composites, J. Am. Ceram. Soc. 91 (2008) 3434–3436, https://doi.org/10.1111/j.1551-2916.2008.02632.x.

[42] H. Pi, S. Fan, Y. Wang, C/SiC–ZrB2–ZrC composites fabricated by reactive melt infiltration with ZrSi2 alloy, Ceram. Int. 38 (2012) 6541–6548, https://doi.org/10.1016/j.ceramint.2012.05.035.

[43] L. Zou, N. Wali, J.-M. Yang, N.P. Bansal, Microstructural development of a Cf/ZrC composite manufactured by reactive melt infiltration, J. Eur. Ceram. Soc. 30 (2010) 1527–1535, https://doi.org/10.1016/j.jeurceramsoc.2009.10.016.

[44] P. Galizia, D. Sciti, F. Saraga, L. Zoli, Off-axis damage tolerance of fiber-reinforced composites for aerospace systems, J. Eur. Ceram. Soc. 40 (2020) 2691–2698, https://doi.org/10.1016/j.jeurceramsoc.2019.12.038.

[45] R.T. Bhatt, R.E. Phillips, Laminate behavior for SiC fiber-reinforced reaction-bonded silicon nitride matrix composites, J. Compos. Technol. Res. 12 (1990) 13–23, https://doi.org/10.1520/ctr10173j.

[46] J. Koyanagi, H. Hatta, M. Kotani, H. Kawada, A comprehensive model for determining tensile strengths of various unidirectional composites, J. Compos. Mater. 43 (2009) 1901–1914, https://doi.org/10.1177/0021998309341847.

[47] D. Zhang, D.R. Hayhurst, Stress-strain and fracture behaviour of 0°/90° and plain weave ceramic matrix composites from tow multi-axial properties, Int. J. Solids Struct. 47 (2010) 2958–2969, https://doi.org/10.1016/j.ijsolstr.2010.06.023.

[48] V. Rubio, J. Binner, S. Cousinet, G. Le Page, T. Ackerman, A. Hussain, P. Brown, I. Dautremont, Materials characterisation and mechanical properties of Cf-UHTC powder composites, J. Eur. Ceram. Soc. 39 (2019) 813–824, https://doi.org/10.1016/J.JEURCERAMSOC.2018.12.043.

[49] Y. Zhu, X. Meng, Q. Zhang, L. Yan, H. Cui, Preparation and mechanical characteristics of fine-woven cloth and punctured felt preform Cf/C-SiC-ZrC composite, Int. J. Appl. Ceram. Technol. (2021) ijac.13759, https://doi.org/10.1111/ijac.13759.

[50] S. Hofmann, Effect of interlaminar defects on the mechanical behaviour of carbon fibre reinforced silicon carbide (2014).

[51] C. Liu, D. Du, H. Li, Y. Hu, X. Xu, J. Tian, G. Tao, J. Tao, Interlaminar failure behavior of GLARE laminates under short-beam three-point-bending load, Compos. Part B Eng. 97 (2016) 361–367, https://doi.org/10.1016/j.compositesb.2016.05.003.

[52] M. Xie, D.F. Adams, Study of three- and four-point shear testing of unidirectional composite materials, Composites. 26 (1995) 653–659, https://doi.org/10.1016/0010-4361(95)98914-7.

[53] M. Li, R. Matsuyama, M. Sakai, Interlaminar shear strength of C/C-composites: the dependence on test methods, PERGAMON Carbon 37 (1999) 1749–1757, https://doi.org/10.1016/S0008-6223(99)00049-4.

[54] K. Rohwer, Models for Intralaminar damage and failure of fiber composites - a review, Facta Univ. Ser. Mech. Eng. 14 (2016) 1–19, https://doi.org/10.22190/fume1601001r.

[55] A. Yasmin, P. Bowen, Fracture behaviour of cross-ply Nicalon/CAS-II glass-ceramic matrix composite laminate at room and elevated temperatures, Compos. Part A Appl. Sci. Manuf. 33 (2002) 1209–1218, https://doi.org/10.1016/S1359-835X(02)00079-9.

[56] S. Schmidt-Wimmer, S. Beyer, F. Wigger, K. Quering, K. Bubenheim, C. Wilhelmi, Evaluation of ultra high temperature ceramics and coating-systems for their application in orbital and air-breathing propulsion, in: 18th AIAA/3AF Int. Sp. Planes Hypersonic Syst. Technol. Conf. 2012, 2012. https://doi.org/10.2514/6.2012-5908.

[57] G. Motz, S. Schmidt, S. Beyer, The PIP-Process: Precursor Properties and Applications, in: Ceram. Matrix Compos., Wiley-VCH Verlag GmbH & Co. KGaA, Weinheim, Germany, n.d., pp. 165–186. https://doi.org/10.1002/9783527622412.ch7.

[58] J.J. de Pablo, N.E. Jackson, M.A. Webb, L.Q. Chen, J.E. Moore, D. Morgan, R. Jacobs, T. Pollock, D.G. Schlom, E.S. Toberer, J. Analytis, I. Dabo, D.M. DeLongchamp, G.A. Fiete, G.M. Grason, G. Hautier, Y. Mo, K. Rajan, E.J. Reed, E. Rodriguez, V. Stevanovic, J. Suntivich, K. Thornton, J.C. Zhao, New frontiers for the materials genome initiative, Npj Comput. Mater. 5 (2019) 1–23, https://doi.org/10.1038/s41524-019-0173-4.

[59] S.W. Tsai, E.M. Wu, A general theory of strength for anisotropic materials, J. Compos. Mater. 5 (1971) 58–80, https://doi.org/10.1177/002199837100500106.

[60] E.P. Popov, Introduction to mechanics of solids, Prentice-Hall, Englewood Cliffs, N.J., 1963. https://trove.nla.gov.au/work/10762419?q&versionId=19182875 (accessed January 13, 2020).

[61] W. Van, P. Guaep, Development and finite element implementation of a damage model for fatigue of fibre-reinforced polymers, Ghent University Architectural and Engineering Press, 2002.

[62] K.S. Liu, S.W. Tsai, A progressive quadratic failure criterion for a laminate, Compos. Sci. Technol. 58 (1998) 1023–1032, https://doi.org/10.1016/S0266-3538(96)00141-8.

[63] W. Van Paepegem, J. Degrieck, Calculation of damage-dependent directional failure indices from the Tsai - Wu failure criterion, Compos. Sci. Technol. 63 (2003) 305–310, https://doi.org/10.1016/S0266-3538(02)00251-8.

[64] S. Li, E. Sitnikova, Y. Liang, A.S. Kaddour, The Tsai-Wu failure criterion rationalised in the context of UD composites, Compos. Part A Appl. Sci. Manuf. 102 (2017) 207–217, https://doi.org/10.1016/j.compositesa.2017.08.007.

[65] P. Morgan, Carbon Fibers and their Composites, Taylor & Francis, 2005.

[66] W.-C. Tu, F.F. Lange, A.G. Evans, Concept for a damage-tolerant ceramic composite with "strong" interfaces, J. Am. Ceram. Soc. 79 (1996) 417–424, https://doi.org/10.1111/j.1151-2916.1996.tb08138.x.

[67] E.A.V. Carelli, H. Fujita, J.Y. Yang, F.W. Zok, Effects of thermal aging on the mechanical properties of a porous-matrix ceramic composite, J. Am. Ceram. Soc. 85 (2004) 595–602, https://doi.org/10.1111/j.1151-2916.2002.tb00138.x.

[68] J.P. Singh, N.P. Bansal, T. Goto, J. Lamon, S.R. Choi, M.M. Mahmoud, G. Link, Processing and Properties of Advanced Ceramics and Composites IV, John Wiley & Sons, Inc., Hoboken, NJ, USA, 2012. https://doi.org/10.1002/9781118491867.

[69] K. Triantou, K. Mergia, S. Florez, B. Perez, J. Barcena, W. Rotärmel, G. Pinaud, W. P.P.P.P. Fischer, Thermo-mechanical performance of an ablative/ceramic composite hybrid thermal protection structure for re-entry applications, Compos. Part B Eng. 82 (2015) 159–165, https://doi.org/10.1016/j.compositesb.2015.07.020.

[70] W. Krenkel, Ceramic Matrix Composites: Fiber Reinforced Ceramics and their Applications, 2008. https://doi.org/10.1002/9783527622412.

[71] K.I. Triantou, K. Mergia, B. Perez, S. Florez, A. Stefan, C. Ban, G. Pelin, G. Ionescu, C. Zuber, W.P.P. Fischer, J. Barcena, Thermal shock performance of carbon-bonded carbon fiber composite and ceramic matrix composite joints for thermal protection re-entry applications, Compos. Part B Eng. 111 (2017) 270–278, https://doi.org/10.1016/j.compositesb.2016.12.020.

[72] K. Triantou, K. Mergia, A. Marinou, G. Vekinis, J. Barcena, S. Florez, B. Perez, G. Pinaud, J.M. Bouilly, W.P.P. Fischer, Novel hybrid ablative/ceramic layered composite for earth re-entry thermal protection: microstructural and mechanical performance, J. Mater. Eng. Perform. 24 (2015) 1452–1461, https://doi.org/10.1007/s11665-015-1410-8.

[73] M. Berbon, M. Calabrese, Effect of 1600°C heat treatment on C/SiC composites fabricated by polymer infiltration and pyrolysis with allylhydridopolycarbosilane, J. Am. Ceram. Soc. 85 (2004) 1891–1893, https://doi.org/10.1111/j.1151-2916.2002.tb00374.x.

[74] G.D. Sorarù, L. Pederiva, J. Latournerie, R. Raj, Pyrolysis kinetics for the conversion of a polymer into an amorphous silicon oxycarbide ceramic, J. Am. Ceram. Soc. 85 (2002) 2181–2187, https://doi.org/10.1111/j.1151-2916.2002.tb00432.x.

[75] L. Zoli, D. Sciti, L.-A. Liew, K. Terauds, S. Azarnoush, R. Raj, Additive manufacturing of ceramics enabled by flash pyrolysis of polymer precursors with nanoscale layers, J. Am. Ceram. Soc. 99 (2016) 57–63, https://doi.org/10.1111/jace.13946.

[76] L. Chen, X. Yang, Z. Su, C. Fang, G. Zeng, Q. Huang, Fabrication and performance of micro-diamond modified C/SiC composites via precursor impregnation and

pyrolysis process, Ceram. Int. 44 (2018) 9601–9608, https://doi.org/10.1016/j.ceramint.2018.02.185.

[77] C.L. Su, Y.Y. Zhou, K. Jiang, F.H. Yang, H.Z. Xu, C.L. Zhou, F.T. Liu, Effect of pyrolytic carbon coating on properties of Cf/C-SiC-ZrC ceramic matrix composites, Mater. Sci. Eng. 678 (2019), https://doi.org/10.1088/1757-899X/678/1/012067 012067.

[78] B. Harris, E. Institute of Materials (London, Engineering composite materials, IOM, London, 1999. https://books.google.it/books/about/Engineering_Composite_Materials.html?id=9MVRAAAAMAAJ&redir_esc=y (accessed November 24, 2017).

[79] K. Naito, Y. Tanaka, J.-M. Yang, Y. Kagawa, Flexural Properties of PAN-and Pitch-Based Carbon Fibers, (n.d.). https://doi.org/10.1111/j.1551-2916.2008.02868.x.

[80] R. Potluri, Mechanical properties evaluation of T800 carbon fiber reinforced hybrid composite embedded with silicon carbide microparticles: a micromechanical approach, Multidiscip. Model. Mater. Struct. 14 (2018) 589–608, https://doi.org/10.1108/MMMS-09-2017-0106.

[81] R. Maurin, P. Davies, N. Baral, C. Baley, Transverse properties of carbon fibres by nano-indentation and micro-mechanics, Appl. Compos. Mater. 15 (2008) 61–73, https://doi.org/10.1007/s10443-008-9057-3.

[82] R.J. D'Mello, A.M. Waas, Influence of unit cell size and fiber packing on the transverse tensile response of fiber reinforced composites, Materials (Basel) 12 (2019), https://doi.org/10.3390/ma12162565.

[83] I. Krucinska, T. Stypka, Direct measurement of the axial Poisson's ratio of single carbon fibres, Compos. Sci. Technol. 41 (1991) 1–12, https://doi.org/10.1016/0266-3538(91)90049-U.

[84] S. Behzadi, M. Imani, M. Yousefi, Prediction of elastic properties of pyrolytic carbon based on orientation angle related content pyrolytic carbon coating for cytocompatibility of titanium oxide nanoparticles: a promising candidate for medical applications, Conf. Ser. Mater. Sci. Eng. 213 (2017), https://doi.org/10.1088/1757-899X/213/1/012030 012030.

[85] F. Monteverde, S. Guicciardi, A. Bellosi, Advances in microstructure and mechanical properties of zirconium diboride based ceramics, Mater. Sci. Eng. A 346 (2003) 310–319, https://doi.org/10.1016/S0921-5093(02)00520-8.

[86] S.R. Shah, R. Raj, Mechanical properties of a fully dense polymer derived ceramic made by a novel pressure casting process, Acta Mater. 50 (2002) 4093–4103, https://doi.org/10.1016/S1359-6454(02)00206-9.

[87] R. Gaillac, P. Pullumbi, F.X. Coudert, ELATE: An open-source online application for analysis and visualization of elastic tensors, J. Phys. Condens. Matter. 28 (2016), https://doi.org/10.1088/0953-8984/28/27/275201 275201.

[88] L.J. Walpole, On bounds for the overall elastic moduli of inhomogeneous systems—II, J. Mech. Phys. Solids 14 (1966) 289–301.

[89] P. Galizia, L. Zoli, D. Sciti, Impact of residual stress on thermal damage accumulation, and Young's modulus of fiber-reinforced ultra-high temperature ceramics, Mater. Des. 160 (2018) 803–809, https://doi.org/10.1016/J.MATDES.2018.10.019.

[90] Y. Lin, C. Liu, H. Li, K. Jin, J. Tao, Interlaminar failure behavior of GLARE laminates under double beam five-point-bending load, Compos. Struct. 201 (2018) 79–85, https://doi.org/10.1016/j.compstruct.2018.06.037.

[91] D. Koch, Microstructural Modeling and Thermomechanical Properties, in: Ceram. Matrix Compos., Wiley-VCH Verlag GmbH & Co. KGaA, Weinheim, Germany, n.d., pp. 231–259. https://doi.org/10.1002/9783527622412.ch10.